

Hydrogen-enhanced vacancy embrittlement of grain boundaries in ironHiroyoshi Momida,^{1,2,*} Yusuke Asari,^{1,†} Yoshimichi Nakamura,^{1,‡} Yoshitaka Tateyama,^{3,4} and Takahisa Ohno^{1,5,6,§}¹*Computational Materials Science Unit, National Institute for Materials Science, 1-2-1 Sengen, Tsukuba, Ibaraki 305-0047, Japan*²*Institute of Scientific and Industrial Research, Osaka University, 8-1 Mihogaoka, Ibaraki, Osaka 567-0047, Japan*³*International Center for Materials Nanoarchitectonics, National Institute for Materials Science, 1-1 Namiki, Tsukuba, Ibaraki 305-0044, Japan*⁴*PRESTO, Japan Science and Technology Agency (JST), 4-1-8 Honcho, Kawaguchi, Saitama 333-0012, Japan*⁵*Global Research Center for Environment and Energy based on Nanomaterials Science, National Institute for Materials Science, 1-2-1 Sengen, Tsukuba, Ibaraki 305-0047, Japan*⁶*Institute of Industrial Science, University of Tokyo, 4-6-1 Komaba, Meguro, Tokyo 153-8505, Japan*

(Received 19 July 2012; revised manuscript received 21 August 2013; published 21 October 2013)

We have investigated atomistic and electronic mechanisms of hydrogen embrittlement at grain boundaries of iron in the presence and absence of vacancies by using first-principles calculations. Considering interactions between hydrogen, vacancies, and $\Sigma 3$ grain boundaries in α -Fe, we have searched for the most deleterious defect states by evaluating their influence on tensile strength under static tensile strain. The calculated results show that hydrogen and vacancies prefer to accumulate as defect complexes near grain boundaries, thereby decreasing the tensile strength of grain boundaries. Theoretical stress-strain curves show that a strength lowering at grain boundaries by the defect complexes is found to be much worse than the effect of each factor. Because of the low mobility of vacancies, this mechanism can account for the delayed brittle fractures induced by hydrogen in steel materials.

DOI: [10.1103/PhysRevB.88.144107](https://doi.org/10.1103/PhysRevB.88.144107)

PACS number(s): 62.20.mj, 81.05.Bx

I. INTRODUCTION

Hydrogen embrittlement (HE) in steels, known as a cause of delayed fractures of high-strength steels, has been a long standing problem, and the atomistic mechanisms of HE have not been fully understood yet.¹⁻⁶ This problem is associated with many different materials including added elements, external environments such as temperature and loading, and microscopic structures of materials. At the atomic scale, interactions between H and Fe, H and defects, and accumulation of a large amount of H at voids or lattice defects can all have effects on embrittlement.¹⁻⁶ Leading theories of HE include the H-enhanced local plasticity⁷ and the H-enhanced decohesion⁸ models, which are developed by considering atomic and electronic interactions between H in Fe and defects such as point defects, grain boundaries, and dislocations. Recently, more practical continuum models of HE are suggested with considering many contributing parameters such as H diffusions and temperatures and so on.⁹ However, an atomic-scale deterioration mechanism in steels, which probably depends on the materials and their environments, is still under discussion.

For high-strength steels, experiments have shown that maximum tensile stress decreases with increasing H content in the materials,¹⁰ and in many cases, fractography shows grain-boundary (GB) fractures induced by H.¹⁰⁻¹² In the most recent and in some advanced cases, grain sizes of steel materials have become smaller and smaller reaching less than 1 μm with controlling types of GBs, to improve material strength.⁶ Thus understanding of HE mechanisms at GB regions becomes increasingly important, and the most deteriorating atomistic factors among complex processes involving many proposed mechanisms need to be clarified, focusing attention on GB regions.

One question is how interstitial H (H^{int}) influences the mechanical strength of a GB. Such knowledge is particularly important for preventing delayed fractures,^{1,3,5} which occur under sustained loads and cold environments, in spite of the light hydrogen, which is considered to be diffusive.⁵ An attractive hypothesis for H-induced GB fractures is that H^{int} in Fe at GB reduces the work of fracture, which is an energy difference between a GB and two fractured surfaces.^{2,3,13,14} Previous first-principles calculations of Fe GBs have clearly shown that GB regions are stronger trap sites for H^{int} than the bulk interstitial sites, and the trapped H^{int} at GBs reduces the work of fracture.¹⁵⁻¹⁸ To understand the H^{int} effects on the GB strength more precisely, a mechanism requires a rigorous link to interatomic bond-breaking behaviors, as pointed out in literature,^{2,3} which is an important property especially under tensile strain.

From another viewpoint, it has long been recognized that there exist Fe vacancies (V^{Fe}), which interact with H in steels.²⁻⁵ Thanks to recent technical advances, both experimental¹⁹⁻²⁴ and computational²⁵⁻³⁰ studies have shown the significance of V^{Fe} in the presence of H. It has been experimentally reported that strain and plastic deformation can create a huge amount of vacancies inside steel materials, which can be present in much higher concentration than the thermal equilibrium values.²² It has also been experimentally shown that such vacancy creations inside the materials are drastically enhanced by H.^{20,24} First-principles calculations have shown that H energetically stabilizes V^{Fe} by coupling as point-defect complexes,²⁵⁻³⁰ and this is also considered as a reason of the superabundant vacancy formation phenomena.^{20,21} In addition, theoretical calculations have shown attractive interactions between V^{Fe} s and GBs in Fe,³¹⁻³³ and V^{Fe} at GBs significantly influences V^{Fe} -migration and GB-sliding properties in the materials.^{32,33} These findings suggest that V^{Fe} has a potential

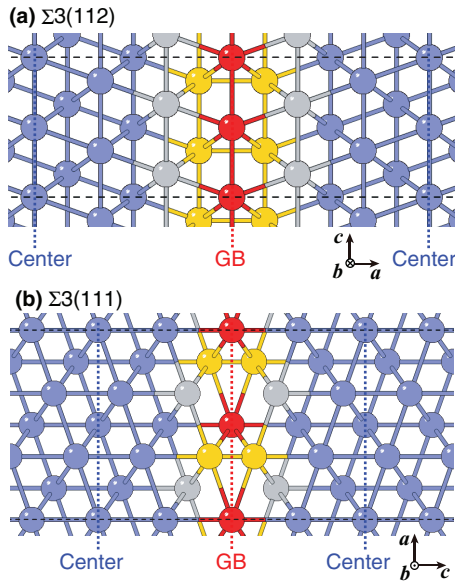


FIG. 1. (Color online) Atomic structures of the pristine (a) $\Sigma 3(112)$ and (b) $\Sigma 3(111)$ symmetric tilt grain boundary (GB) models. The GB Fe atoms within five layers are highlighted by red, yellow, and gray for the GB, GB-1, and GB-2 layer atoms, respectively.

influence in HE, but its actual effect on mechanical tensile strength is not yet clear. Therefore it is important to know how H and GB interact in Fe with, and without, the presence of V^{Fe} , and how they influence mechanical strength.

In this study, using first-principles calculations, realistic defect-structures for H, V^{Fe} , and $\Sigma 3$ GBs in α -Fe are investigated by energy analyses considering potential multiple-defect configurations. Then the influence of H^{int} , V^{Fe} , and V^{Fe} with H atoms on GB strength is assessed by using tensile test calculations under static uniaxial strain perpendicular to the GB planes, in which the elongation-breaking behavior of electronic bonds is explicitly considered. Comparing the calculated stress-strain curves, we find an atomistic and electronic mechanism for significant GB weakening in α -Fe, which is induced by the coupling effects of H and V^{Fe} . Calculated results show that H stabilizes V^{Fe} at GBs, and the V^{Fe} -H complexes ($V^{\text{Fe}}\text{H}_n$, where n is the number of trapped H at a V^{Fe}) accumulated at GBs significantly reduce the tensile strength of GBs, resulting in them locally becoming much weaker planes inside the materials. In comparison with H^{int} at GBs with realistic concentrations, this deterioration of GB strength by $V^{\text{Fe}}\text{H}_n$ is much worse than that by H^{int} , and is more selective to the type of GB involved.

II. MODELS AND METHODS

A. Grain boundary models

Figure 1 shows atomic structures of GB models used in this study. We use the periodic supercell models of two symmetric tilt GBs which are modeled on the basis of the coincidence site lattice theory: $\Sigma 3(112)$ GB having a dense GB structure and $\Sigma 3(111)$ GB having an intrinsic open space at GB.^{31,34} The local environment of Fe at GB in $\Sigma 3(112)$ is the distorted eight coordination, relatively similar to that in bulk. In $\Sigma 3(111)$, the Fe atoms of GB-1 layers across the GB layer

are closed relative to the Fe-Fe distance in the bulk. $\Sigma 3(112)$ and $\Sigma 3(111)$ are known to have much lower and higher GB energies among the symmetric tilt GBs of α -Fe, respectively, and the smaller and larger local-structural units at the GBs can be considered as basic structure units for modeling other local GB-structures.^{31,34} Considering such GB characters, the $\Sigma 3(112)$ and the widely-used $\Sigma 3(111)$ GB models may be considered as a model for the major component of the system and for a trigger region of a fracture, respectively.

We use orthorhombic supercell models of both the pristine GBs composed of 96 Fe atoms per unit cell. Both supercells have 24 layers/cell in a direction perpendicular to the GB plane and have two GBs in the cell due to the periodicity. The cell lengths (a, b, c) for the $\Sigma 3(112)$ and the $\Sigma 3(111)$ GBs are $(4\sqrt{6}a_{\text{bulk}}, 2\sqrt{2}a_{\text{bulk}}, \sqrt{3}a_{\text{bulk}})$ and $(\sqrt{6}a_{\text{bulk}}, 2\sqrt{2}a_{\text{bulk}}, 4\sqrt{3}a_{\text{bulk}})$, in which GB planes are perpendicular to the a and c axes, respectively. Here, a_{bulk} is the lattice constant of α -Fe. We use the calculated a_{bulk} value of 2.837 Å as shown in the next section, thus the supercell sizes are (27.797, 8.024, 4.914) and (6.949, 8.024, 19.655) in angstroms having the GB areas of 39.43 and 55.76 Å²/cell for $\Sigma 3(112)$ and $\Sigma 3(111)$, respectively.

B. First-principles calculations

The first-principles calculations are based on the density functional theory (DFT)^{35,36} within the generalized gradient approximation (GGA) of the Perdew-Burke-Ernzerhof exchange-correlation functional (PBE),³⁷ and the Kohn-Sham equations are solved self-consistently using the projector augmented wave method (PAW)^{38,39} under periodic boundary condition. Computations are performed using the Vienna *ab initio* simulation package (VASP).^{40,41} The real-space method is used for the projection operators, and the first-order Methfessel-Paxton scheme with a smearing width 0.2 eV is used for the Brillouin-zone integration.⁴² The cutoff energy is set to 334.9 eV for the plane-wave basis set and 511.4 eV for the augmentation charges. The convergence criteria of self-consistent calculations are set to 1×10^{-5} eV/cell for the total energy, and that of structure relaxations are set to less than 5×10^{-2} eV/Å for the atomic forces. The charge density distributions shown in this paper are visualized by utilizing the computer software VMD.⁴³

C. Bulk and pristine grain boundaries

As listed in Table I, we have checked calculation accuracies for the ferromagnetic α -Fe perfect crystal using the Γ -centered sampling \mathbf{k} mesh $12 \times 12 \times 12$. Our calculated values of lattice constant 2.837 Å, bulk modulus 179 GPa, which are calculated by the DFT total energies least-square-fitted to Murnaghan's equation of state, and spin magnetic moment of 2.26 μ_{B} /Fe are consistent with previous DFT-GGA calculations^{17,18,25,32,44-46} and experiments.^{47,48} We use the calculated lattice constant in this study.

In Table I, we also list defect formation energies (E^{f}) of H^{int} and V^{Fe} calculated using the bulk 128-atom cubic supercell of α -Fe using the $2 \times 2 \times 2$ \mathbf{k} mesh, here E^{f} s are referenced to the gaseous H_2 molecule and pure Fe calculated using the same supercell size. There are tetrahedral and octahedral trap

TABLE I. Calculated values of ferromagnetic bulk α -Fe comparing with experiments and other DFT-GGA calculations for lattice constant (a), bulk modulus (B), and spin magnetic moment (M). Vacancy formation energy [$E^f(\text{V}^{\text{Fe}})$] and formation energy (heat of solution) of interstitial hydrogen at the tetrahedral site [$E^f(\text{H}^{\text{int}})$] are calculated using the 128-atom cubic supercell of the bulk.

	Our calculation	Other DFT-GGA calculations	Experiments
a (Å)	2.837	2.83–2.86 ^{17,18,25,32,44,45}	2.87 ⁴⁷
B (GPa)	179	152–174 ^{25,45,46}	168.3 ⁴⁷
M (μ_{B}/Fe)	2.26	2.20–2.32 ^{25,45,46}	2.216 ⁴⁸
$E^f(\text{H}^{\text{int}})$ (eV/H)	0.21	0.20–0.25 ^{17,18,46} , (0.30–0.34 ^{25,46}) ^a	0.296 ³
$E^f(\text{V}^{\text{Fe}})$ (eV/V ^{Fe})	2.15	1.95–2.14 ^{25,32,45}	1.4–2.0 ^{21,49–51}

^aValues in the parenthesis include the zero-point motion energies of hydrogen, which is not included in our calculations.

sites (T and O sites) for H^{int} in the bulk environment, and the calculated E^f of H^{int} are 0.21 and 0.34 eV/H for the T and O sites, respectively, showing that the T site is more stable.²⁵ The calculated E^f of V^{Fe} is 2.15 eV/V^{Fe}. Our calculations of the defects in bulk show good agreement with the previous DFT studies,^{17,18,25,32,45,46} and close to the experimental values listed in Table I.^{3,21,49–51}

For the $\Sigma 3(112)$ and the $\Sigma 3(111)$ GB models, the Γ -centered sampling \mathbf{k} meshes in the Brillouin zone of $1 \times 4 \times 4$ and $4 \times 4 \times 1$ are used, respectively. The GB energy (γ_{GB}) of a pristine GB is calculated as

$$\gamma_{\text{GB}} = \frac{E_{\text{GB}} - E_{\text{bulk}}}{2S_{\text{GB}}}, \quad (1)$$

where E_{GB} and E_{bulk} are the DFT total energies of GB and bulk calculated with the same 96-atom orthorhombic supercell size, respectively, and S_{GB} is the area of GB in the unit cell that contains two GBs. The calculated γ_{GB} listed in Table II of the $\Sigma 3(112)$ and the $\Sigma 3(111)$ GBs are 0.44 and 1.66 J/m², showing lower- and higher-energy GBs, respectively, which are consistent with the reported theoretical values^{31,34} and close to the previous DFT calculations.^{16–18,44}

D. Formation energy of defects

To find most stable defect structures, we calculate the formation energy (E^f) of a defect composed of $n\text{V}^{\text{Fe}}$ and $m\text{H}$ in the cell (denoted as $\text{V}_n^{\text{Fe}}\text{H}_m$, n and m are the number of each

defects per cell) as

$$E^f(\text{V}_n^{\text{Fe}}\text{H}_m) = E_{\text{GB}}(\text{Fe}_{N-n}\text{V}_n^{\text{Fe}}\text{H}_m) - E_{\text{GB}}(\text{Fe}_N) + \frac{n}{N}E_{\text{bulk}}(\text{Fe}_N) - \frac{m}{2}E_{\text{gas}}(\text{H}_2), \quad (2)$$

here the number of Fe atoms $N = 96$ atom/cell in our models. E_{GB} , E_{bulk} , and E_{gas} are the DFT total energies of the GB, the bulk, and the gaseous H_2 molecule, which are calculated using the same unit-cell size.

We search for the most probable defect structures, which have the lowest E^f for V_1^{Fe} , H_1 , $\text{V}_1^{\text{Fe}}\text{H}_1$, and $\text{V}_1^{\text{Fe}}\text{H}_2$, as a function of distance from the GB with considering configurations and distances of V^{Fe} and H atoms. As a result of most-stable locations of H at V^{Fe} , cluster structures of $\text{V}_1^{\text{Fe}}\text{H}_1$ and $\text{V}_1^{\text{Fe}}\text{H}_2$ at GBs are basically similar to the previously reported $\text{V}_n^{\text{Fe}}\text{H}_m$ cluster structures in bulk α -Fe.^{25,27}

The calculated lowest E^f values within the present study are summarized in Table III; all of the defects are more stable near GBs relative to the bulk, as discussed later in the results sections. Note that the bulk formation energies listed in Table III are calculated using the bulk 96-atom orthorhombic supercell, which has the same cell size as the $\Sigma 3(112)$ GB supercell. The energy difference relative to the bulk 128-atom cubic supercell (Table I) show rather weak interactions between defects of neighboring cells within 0.03 eV, thus a single defect in the present supercells has basically the property of isolated defects on GBs.

E. Models and methods of tensile-test calculations

First-principles studies of mechanical strength have provided us useful information, for example, about the ideal shear strength of Al and Cu,⁵² effects of Bi on the GB strength of Cu,⁵³ embrittlement of Ni GB by S segregations,⁵⁴ and Na-induced embrittlement of Al GB.⁵⁵ Based on the reported simulation methods of first-principles tensile tests, we evaluate the effect of defects on tensile strength at GBs under uniaxial tensile strain. For the tensile-test calculations, we use slab models of GB with and without the defects. The following procedure of tensile tests is applied in the same way for all of the GB models with/without defects, considering elongation-breaking behaviors of bonds as accurately as possible, and we use the same calculation conditions for our purpose of comparison between the models.

(1) We prepare a slab model that is composed of a test specimen including the GB, held between two grips. The test specimen is seven layers of the GB with/without a defect, which is extracted from the GB model used for the defect

TABLE II. Calculated grain boundary energies (γ_{GB}) and works of fracture (cohesive energies) (2γ) of the pristine $\Sigma 3(112)$ and $\Sigma 3(111)$ grain boundary models.

	GB type	Our calculation	Other DFT-GGA calculations	Other theories
γ_{GB} (J/m ²)	$\Sigma 3(112)$	0.44	0.47 ¹⁸	0.267 ^a , 0.262 ^b
	$\Sigma 3(111)$	1.66	1.52 ¹⁷ , 1.61 ⁴⁴	1.23 ^a , 1.297 ^b
2γ (J/m ²)	$\Sigma 3(112)$	4.66	4.93 ¹⁸	
	$\Sigma 3(111)$	3.65	3.86 ¹⁶	

^aReference 34, classical potential calculations.

^bReference 31, molecular statics simulations.

TABLE III. Calculated lowest formation energies of interstitial hydrogen (H^{int}), iron vacancy (V^{Fe}), and vacancy-hydrogen complexes ($V^{\text{Fe}}H_n$, $n = 1$ and 2) at bulk, $\Sigma 3(112)$, $\Sigma 3(111)$ and the reconstructed $\Sigma 3(111)$ [re- $\Sigma 3(111)$, Fig. 16] grain boundary models.

(eV/f.u.)	H^{int}	V^{Fe}	$V^{\text{Fe}}H_1$	$V^{\text{Fe}}H_2$
Bulk ^a	0.18	2.12	1.73	1.31
$\Sigma 3(112)$	-0.10	1.73	1.36	0.98
$\Sigma 3(111)$	-0.19	-0.22	-0.28	-0.46
re- $\Sigma 3(111)$	-0.15	0.67	0.28	-0.06

^aListed bulk values are calculated using the 96-atom bulk orthorhombic supercell, which has the same cell size as the $\Sigma 3(112)$ model. Differences from the bulk values listed in Table I show a rather small cell-size dependence within 0.03 eV/f.u. For the 96-atom bulk supercell, which has the same cell-size as the $\Sigma 3(111)$ model, calculated formation energies are 0.18 eV/H, 2.16 eV/ V^{Fe} , 1.76 eV/ $V^{\text{Fe}}H_1$, and 1.32 eV/ $V^{\text{Fe}}H_2$, respectively.

energy analyses. The test specimen is inserted between two grips that are respectively bulk-terminated three layers having the same plane orientation, thus atomic structures between the test specimen and the grips are naturally connected in a seamless manner. The GB plane is parallel to the slab, and the slab is placed in a vacuum. The unit cell has the same size as that used in the energy analysis, and is fixed during the tensile test.

(2) The slab thickness is optimized, and the atomic positions except for the grip atoms are relaxed to remove any artificial strain. Thus the model is set in its equilibrium structure, which is defined as the zero-strain state.

(3) Before doing the tensile test calculations, we search for the most probable fractured surfaces. The slab is artificially cleaved at the GB and is separated by a large enough distance to make two fractured surfaces, and the atomic structures are allowed to fully relax except for the grip atoms. Comparing the DFT total energies for assumed cleavage pathways at the GB, we determine the lowest-energy fracture surface.

(4) The tensile test is carried out using the slab model. The two grips are pulled in opposite directions perpendicular to the GB. For a fixed distance between the two grips (d), which is measured from the equilibrium zero-strain structure ($d = 0$), the atomic structures are fully relaxed except for the grip atoms. Thus the tensile test is done under the static strain. In order to promote a reasonable fracture, especially for the model having the mirror symmetry with respect to the GB plane, the model structures are forced to adopt a lower symmetry. For generating the initial structure at d , the test specimen is divided at the probable fractured surface, estimated by (3), and displaced in opposite directions respectively with each of the grips. By repeating this procedure as a function of d , the tensile stress-strain curves are obtained. One of the limitations of this method is that the Poisson contraction is completely neglected.

(5) We define the energy difference as a function of d per unit area [$U(d)$] as

$$U(d) = \frac{E(d) - E(0)}{S_{\text{GB}}}, \quad (3)$$

where $E(d) - E(0)$ is the DFT total energies of the slab models at d relative to that at $d = 0$, and S_{GB} is the area of the GB. The tensile strain [$\varepsilon(d)$] is defined as

$$\varepsilon = d/L, \quad (4)$$

where L is the equilibrium thickness of the test-specimen region between the two grips. The tensile stress [$\sigma(d)$] can be calculated as

$$\sigma(d) = \sum_{i \in \text{grip}} \frac{F_i}{S_{\text{GB}}}, \quad (5)$$

where F_i is the atomic force (component normal to the GB) acting on the i th grip atom. We can also calculate $\sigma(d)$ by differentiating $U(d)$ with respect to d as

$$\sigma(d) = \frac{dU(d)}{dd}, \quad (6)$$

and we plot tensile U - ε and σ - ε curves.

The calculated maximum tensile stresses (σ_{max}) of the pristine $\Sigma 3(112)$ and $\Sigma 3(111)$ GBs are 25.1 and 22.3 GPa at the maximum tensile strain (ε_{max}) of 0.22 and 0.25, which correspond to $d = 0.206$ and 0.165 nm, respectively. σ_{max} values calculated by the first-principles tensile-tests, in which several effects such as dislocation motions in real materials are neglected, are typically 1 or 2 orders higher than the experimental σ_{max} of real steel materials. Although it is difficult to provide quantitative comparison with experiments for real steel materials, calculated stress-strain curves give us an ideal strength, which is an important concept to understand mechanical properties of materials.^{52,56,57} The present tensile tests can give us information about the influence of defects on the strength by comparing between the models with/without the defects.

As previously discussed for effects of P, B, and H on Fe GB cohesion from first principles,^{15-18,58} one important index to characterize tensile strength is the work of fracture 2γ ,¹³ which is defined as a difference between a GB energy γ_{GB} and two fractured-surface energies $2\gamma_{\text{surf}}$,

$$2\gamma = 2\gamma_{\text{surf}} - \gamma_{\text{GB}}. \quad (7)$$

The 2γ value of a pristine GB can be calculated as the U at infinite d (at the largest d in the unit cell). As listed in Table II, the calculated values of 2γ of the pristine $\Sigma 3(112)$ and $\Sigma 3(111)$ are 4.66 and 3.65 J/m², respectively, consistent with that of the reported DFT calculations.^{16,18} The 2γ values indicate that the GB strength of $\Sigma 3(111)$ is lower than that of $\Sigma 3(112)$. The calculated γ_{surf} values are 2.65 J/m² for (111) surface and 2.55 J/m² for (112) surface showing a small difference. Thus the much higher γ_{GB} value of $\Sigma 3(111)$ contributes to decrease the 2γ . Another important index is the elastic modulus that is defined as the slope of stress-strain curve at zero strain,

$$E^Y = \left(\frac{d\sigma}{d\varepsilon} \right)_{\varepsilon=0}. \quad (8)$$

Calculated E^Y values of the pristine $\Sigma 3(112)$ and $\Sigma 3(111)$ are 204 GPa and 198 GPa, respectively. Near the maximum of stress-strain curves, nonlinear effects are not negligible as shown later. Here, we note again that effects of the Poisson contraction are not included in this study.

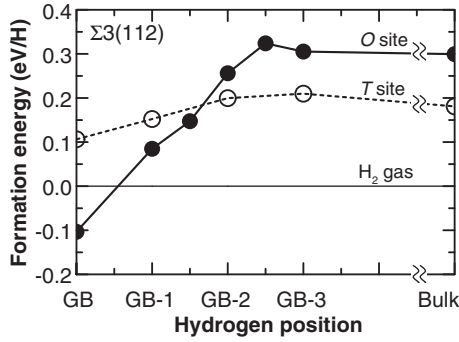


FIG. 2. Formation energies of a single interstitial hydrogen (H^{int}) at the $\Sigma 3(112)$ grain boundary. Closed and open circles are for H^{int} in octahedral (O) and tetrahedral (T) positions, respectively.

III. RESULTS OF $\Sigma 3(112)$ GRAIN BOUNDARY

A. Interstitial hydrogen

1. Accumulation of hydrogen at grain boundary

We start by reporting our results on the influence of H^{int} at the $\Sigma 3(112)$ GB in the absence of V^{Fe} . Figure 2 shows calculated formation energies (E^f s) of a single H^{int} . In the bulk α -Fe, H energetically prefers the interstitial tetrahedral site (T site),²⁵ for which calculated E^f is about 0.2 eV/H. The H gains energy stability by moving from the bulk to the GB, and the octahedral coordination site (O site) at the GB center is the most stable position, having an E^f value that is about 0.3 eV/H lower than that at the bulk T site. This result is consistent with the previous work by Du *et al.*, which extensively studied interactions between H^{int} and GBs in Fe from first principles.¹⁸

Figure 2 shows that there are many potential trapping sites of H^{int} near the pristine GB where E^f is lower than the bulk T site. We can estimate how many H^{int} can accumulate at the GB by filling in the potential trapping sites with H^{int} and by finding the lowest-energy site near the GB as a function of number of trapped H^{int} atoms (n). We calculated the formation energy of H^{int} in the $(n-1)H^{\text{int}}$ -trapped GB model as a function of n as

$$E^f(n\text{-th H}) = E_{\text{GB}}(\text{Fe}_N\text{H}_n) - E_{\text{GB}}(\text{Fe}_N\text{H}_{n-1}) - \frac{1}{2}E_{\text{gas}}(\text{H}_2). \quad (9)$$

The calculations were started from $n = 1$ to 12 sequentially, and the lowest E^f position of H^{int} in the $(n-1)H$ -trapped GB model was searched for each n from unoccupied T and O sites within the five GB layers.

Figure 3 shows the lowest $E^f(n\text{-thH})$ values as a function of n . The E^f values up to four H^{int} /cell shows almost flat and lower than the bulk T site and the H_2 gas values. Therefore four H^{int} /cell can readily accumulate on the GB, corresponding to the fully covered O sites at the GB center. The H^{int} concentration of 4 H^{int} /cell is equal to an area density of 10.1 atom/nm² (areal weight density of 1.69×10^{-17} g H/ μm^2), which is a reasonable value if we compare with the experimental estimation of 2.18×10^{-17} g H/ μm^2 observed in steel.²³ In the 4 H^{int} -trapped GB, the fifth H^{int} will try to occupy the O site at the GB-1 layer, but it will go back into the bulk region, because repulsive interactions with the trapped H^{int} make the formation energy higher than

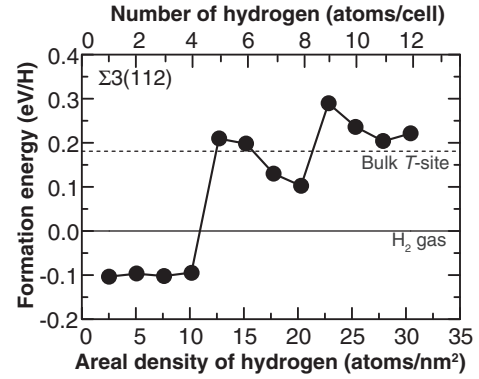


FIG. 3. Lowest formation energies of an interstitial hydrogen (H^{int}) versus number of trapped H^{int} at the $\Sigma 3(112)$ grain boundary. Upper and lower scales show the number of H^{int} per unit cell (H atoms/cell) and the areal number density of H^{int} (H atoms/nm²), respectively.

that for the bulk T site. To accumulate with much higher H^{int} concentrations at GBs, additional mechanisms, such as mobile effects of H during crack propagations, may be necessary as discussed by Yamaguchi *et al.*¹⁷

2. Effects of hydrogen on tensile strength

Figure 4 shows the calculated energy-strain and stress-strain curves of $\Sigma 3(112)$ GBs with and without H^{int} . Figure 4(a) shows that the work of fracture 2γ decreases with increasing number of H^{int} , indicating that H^{int} is a grain-boundary embrittler as reported previously.¹⁵⁻¹⁸ However, we can also

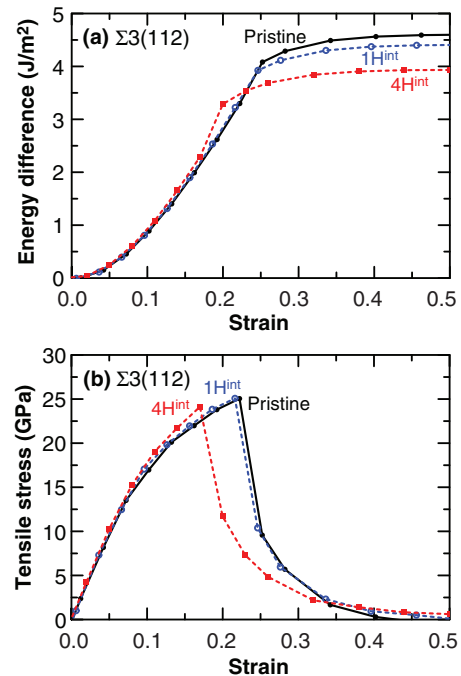


FIG. 4. (Color online) Results of tensile test calculations for the pristine [solid line with closed circles (black)], 1 H^{int} - [broken line with open circles (blue)] and 4 H^{int} -trapped [broken line with squares (red)] $\Sigma 3(112)$ grain boundaries: (a) energy difference relative to the equilibrium and (b) tensile stress vs uniaxial tensile strain.

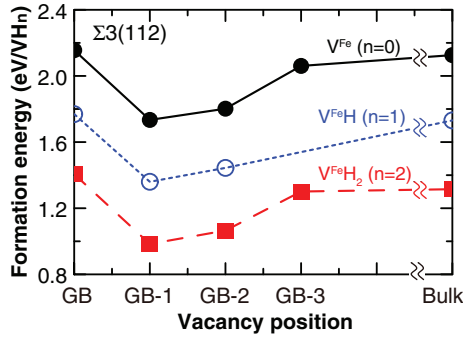


FIG. 5. (Color online) Formation energies of vacancy-hydrogen point-defect complexes $V^{\text{Fe}}\text{H}_n$ ($n = 0-2$) at the $\Sigma 3(112)$ grain boundary. Closed circles (black), open circles (blue), and squares (red) are for $n = 0, 1$, and 2 , respectively.

find that the elastic modulus slightly enhances by accumulating H^{int} at GB, and the slope of stress-strain curves slightly increases with increasing number of H^{int} , especially at larger strains of about 0.1–0.2.

Figure 4(b) shows that the maximum tensile stress (σ_{max}) slightly decreases by accumulating H^{int} , thus H^{int} can have an embrittlement effect at GBs. However, the H^{int} accumulation with the estimated areal density do not drastically reduce σ_{max} at the GB, contrary to our expectations. The effect of a single H^{int} /cell on σ_{max} is almost negligible, and the σ_{max} value is lowered by only 4% even for the four H^{int} /cell accumulation, relative to the pristine $\Sigma 3(112)$ GB ($\sigma_{\text{max}} = 25.1$ GPa).

The maximum tensile strain (ε_{max}), at which electronic bonds connecting the GB are all broken, slightly decreases with an increase in the number of trapped H^{int} . One likely reason for the reduced ε_{max} is that the accumulated H^{int} at GB expands native Fe-Fe bonds at GB at equilibrium structure (zero strain), relative to those in the pristine GB. Such local expansions of Fe-Fe distances at GBs can increase with increasing H^{int} density at GBs, being explained by using the experimental partial molar volume of $0.3 \text{ nm}^3/\text{H}$.^{2,3} Such volume effects of H^{int} might be related to the size effect described for Bi in Cu GB.^{53,59}

B. Vacancy-hydrogen defect complexes

1. Interactions with grain boundary

To clarify the influence of V^{Fe} at the $\Sigma 3(112)$ GB, we evaluate the energy stabilities of V^{Fe} with, and without, H as a function of the distance from the GB by finding the lowest energy structures. Figure 5 shows calculated formation energies of vacancy-hydrogen defect complexes $V^{\text{Fe}}\text{H}_n$ ($n = 0-2$). The lowest E^f of the single V^{Fe} at the GB-1 layer is about $0.4 \text{ eV}/V^{\text{Fe}}$ lower than that in bulk, indicating the presence of attractive interactions between V^{Fe} and GB and the easier creation of V^{Fe} at GB. The $V^{\text{Fe}}\text{H}$ and $V^{\text{Fe}}\text{H}_2$ complexes can be also attracted by the GB from the bulk, and the E^f values at the GB-1 layer lower by about $0.4 \text{ eV}/V^{\text{Fe}}\text{H}$ and about $0.3 \text{ eV}/V^{\text{Fe}}\text{H}_2$ relative to the bulk values, respectively. Thus all the V^{Fe} -related defects tend to accumulate at the GB. Calculated lowest-energy structures of $V^{\text{Fe}}\text{H}$ and $V^{\text{Fe}}\text{H}_2$ defects near GB have the basically similar V^{Fe} -H configurations with that in bulk.²⁵

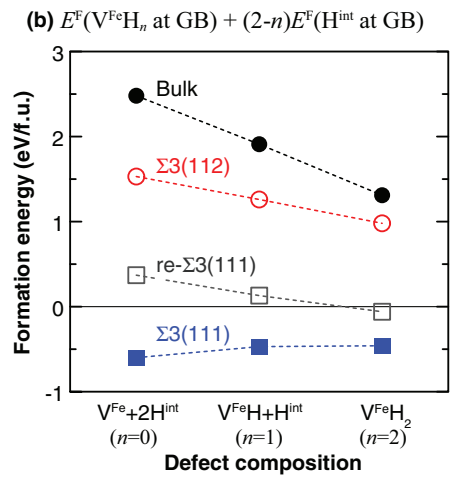
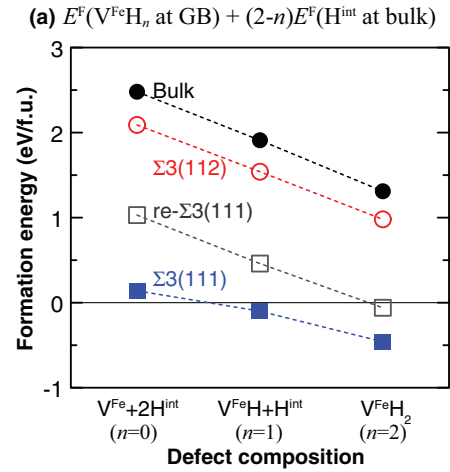


FIG. 6. (Color online) Energy diagram of defects composed of 2H and $1V^{\text{Fe}}$ in the bulk (solid circles), $\Sigma 3(112)$ (open circles), $\Sigma 3(111)$ (solid squares) and the fully reconstructed $\Sigma 3(111)$ (open squares) grain boundary models. Plotted formation energies of GBs are calculated as a sum of the lowest formation energies of $V^{\text{Fe}}\text{H}_n$ and H^{int} at (a) bulk and (b) GBs.

To evaluate what interactions act between a single V^{Fe} and two H^{int} at GB, we compare formation energies of defects composed of 2H and $1V^{\text{Fe}}$ by calculating

$$E^f(V^{\text{Fe}}\text{H}_m) + (2 - m)E^f(\text{H}^{\text{int}}) \quad (10)$$

as a function of $m = 0-2$. In the bulk environment of α -Fe, first-principles studies have shown that V^{Fe} is energetically stabilized by trapping H as shown in Fig. 6, and that the $V^{\text{Fe}}\text{H}_2$ is assigned as a major complex.^{25,27} At a grain boundary, we calculate the formation energies by using $E^f(\text{H}^{\text{int}})$ of H^{int} at bulk and at a grain boundary shown in Figs. 6(a) and 6(b), respectively. We find that V^{Fe} and H are stably coupled as the $V^{\text{Fe}}\text{H}_2$ on the $\Sigma 3(112)$ GB. V^{Fe} s in both the bulk and the GB are stabilized by about 0.6 eV by trapping H^{int} from bulk one by one [see Fig. 6(a)], and the calculated bulk value is close to the experimental value of 0.63 eV ,^{4,21} as discussed in the previous DFT studies.²⁵ V^{Fe} s at the GB can be also stabilized by 0.3 eV by trapping H^{int} of the $\Sigma 3(112)$ -GB O site [see Fig. 6(b)]. The results show that the V^{Fe} -related defects are

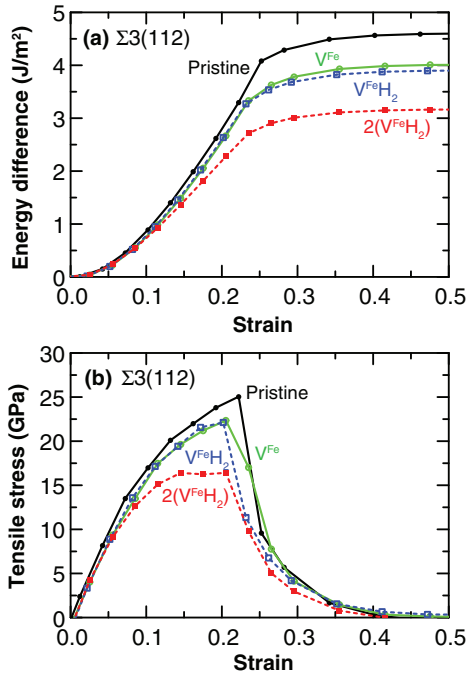


FIG. 7. (Color online) Results of tensile test calculations for the pristine (solid line with closed circles, black), V^{Fe}- (solid line with open circles, green), V^{Fe}H₂- (broken line with open squares, blue) and 2(V^{Fe}H₂)-trapped (broken line with closed squares, red) $\Sigma 3(112)$ grain boundaries: (a) energy difference relative to the equilibrium and (b) tensile stress vs uniaxial tensile strain.

more stable at $\Sigma 3(112)$ GB than that in bulk, and the V^{Fe} at GB is further stabilized by trapping H atoms.

We further considered what interactions act between two V^{Fe}H₂ complexes, and find that they tend to be closer to the GB. The lowest- E^f structure of V^{Fe}H₂-V^{Fe}H₂ complex at the GB is the nearest neighbor in the same GB layer, and the E^f value (0.76 eV/V^{Fe}H₂) is lower than that of the single V^{Fe}H₂ at the GB (0.98 eV/V^{Fe}H₂). This result potentially indicates a strong tendency for the V^{Fe}-related defects to cluster, thereby contributing to initiate the creation of a nanocluster at GB,²⁵ although careful attention associated with a cell-size limitation is required to discuss energy stabilities of larger clusters. Such clusters might contribute to reduce the local tensile strengths of GBs.

2. Effects of vacancy-related defects on tensile strength

Calculated tensile-test results (see Fig. 7) show that the single and the double V^{Fe}H₂ at the GB significantly reduce the σ_{\max} by 12% and 35% respectively, relative to the pristine $\Sigma 3(112)$ GB. These complexes therefore appear to be powerful embrittlers. The σ_{\max} reduction by V^{Fe}H₂ is almost same size as that by V^{Fe}.

Figure 7(a) shows that the V^{Fe}-related defects reduce the work of fracture 2γ . Compared with the effect of V^{Fe} on the 2γ reduction, the 2γ is further reduced by V^{Fe}H₂, and the reduction is more pronounced by double V^{Fe}H₂. Contrary to the H^{int} cases, the elastic modulus before the fracture is also decreased by the V^{Fe}-related defects, contributing to lower σ_{\max} . Thus the V^{Fe}-related defects can have stronger

embrittlement effects at wider range of strain, comparing with H^{int}.

One can speculate that the σ_{\max} reductions originate from missing Fe-Fe bonds which connect the GB caused by the presence of stabilized V^{Fe}. However, the reduction size is significantly enhanced by the V^{Fe}H₂-V^{Fe}H₂ clustering, indicating that they have another degradation mechanism in addition to the simple effect due to number of the missing Fe-Fe bonds. This result suggests that local strengths of GBs become worse and worse with accumulating V^{Fe}-related defects locally at GBs. When compared with the H^{int} cases, the effects of V^{Fe}H₂ on the stress-strain characteristics are distinctly different, especially before fracture, indicating a different nature of the bond breaking processes in the two cases.

C. Analyses of defect influences

1. Griffith theory analysis

To characterize the influence of defects on the GB strength, we consider results based on Griffith's elastic fracture mechanics¹ in which the failure criterion parameters are the elastic modulus E^Y and the work of fracture 2γ , as expressed in

$$\sigma_{\max} = \sqrt{\frac{2\gamma E^Y}{\pi c}} \quad (11)$$

for a crack of length $2c$ without considering plasticity. Here, E^Y and 2γ are the slope and the total area of a stress-strain curve, respectively, and the latter corresponds to the energy difference between a GB and a fractured surface.

As shown in Fig. 4(a), the presence of H^{int} at the GB reduces 2γ , but increases E^Y slightly with an increasing number of trapped H^{int}, indicating that the effects are competitive. The V^{Fe}H₂ complex reduces both 2γ and E^Y as shown in Fig. 7(a), showing its stronger embrittling effects. As an extension of the Petch-Stables surface-energy model,^{2,3,14} the 2γ -reduction effects of H^{int} have been studied precisely from first principles.^{15-18,27} We find that a similar 2γ -reduction effect works also for the V^{Fe}H₂ defect complexes.

2. Charge density analysis

To understand the strength changes produced by the defects from an electronic structure viewpoint, we analyzed the charge densities of the $\Sigma 3(112)$ GB models under static uniaxial strain. Figure 8 shows charge densities of the pristine [see Fig. 8(a)], 4H^{int}-trapped [see Fig. 8(b)], and single and double V^{Fe}H₂-trapped [see Figs. 8(c) and 8(d)] $\Sigma 3(112)$ GB models.

First, let us examine the influence of H^{int}. In Fig. 8(a), at the zero strain, the charge densities at the GB O sites are slightly lower than the bulk interstitial sites, in the pristine $\Sigma 3(112)$ GB. The GB O sites are occupied by the H^{int} atoms in Fig. 8(b), thereby making additional Fe-H^{int}-Fe bonds connecting the GB Fe atoms. Previous studies have shown that the Fe-H bonds have an ionic nature because of electron transfers from Fe to H.^{15,25,27} We can speculate that there are two electronic effects involving bonds that are competitive: the additional Fe-H bonds might more tightly bridge the GB, thereby enhancing elastic strengths, but the native Fe-Fe metallic bonds at the GB might be weakened by an electron-transfer mechanism.¹⁵

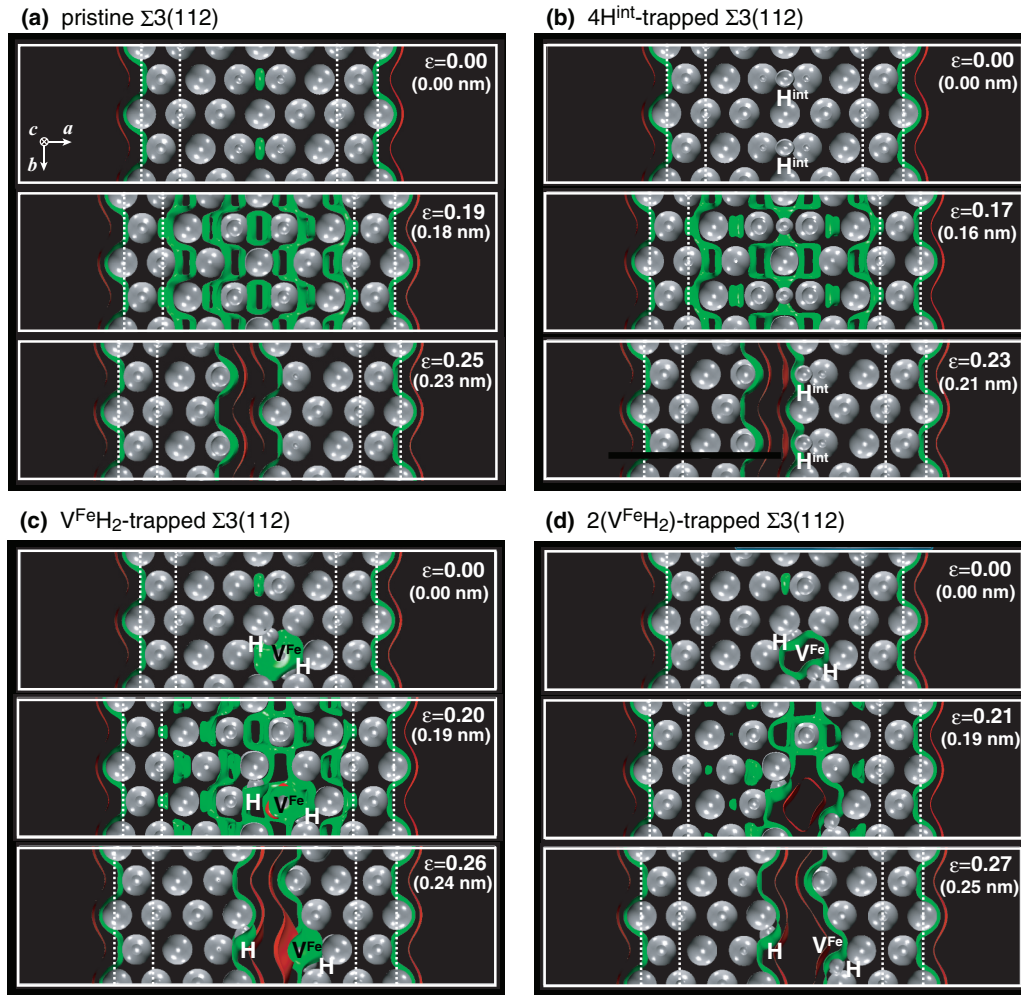


FIG. 8. (Color online) Charge densities under static uniaxial tensile strains of (a) the pristine, (b) 4H^{int} -, (c) the single $\text{V}^{\text{Fe}}\text{H}_2$ -, and (d) $2(\text{V}^{\text{Fe}}\text{H}_2)$ -trapped $\Sigma 3(112)$ grain boundaries. Three isosurfaces of 0.05 (red), 0.2 (green), and $0.5 e/\text{\AA}^3$ (gray) are plotted. Tensile strain (ϵ) is indicated on each panel with the displaced distance (d) of the grips (dotted lines) measured from equilibrium position.

Although it is a subtle problem to accurately determine which effect is dominant, the former seems to be predominant if we consider the enhanced values of E^Y by H^{int} in Fig. 4. Actually, the elastic bond-elongation behavior under strain is rather similar to those of the pristine [the middle panels of Figs. 8(a) and 8(b)], except for the Fe-H-Fe bridging. After the fracture [the lower panels of Figs. 8(a) and 8(b)], it is energetically more preferable for H to locate at the surfaces, and this contributes to the 2γ lowering.^{15–18,27}

The charge densities of the two- $\text{V}^{\text{Fe}}\text{H}_2$ s-trapped $\Sigma 3(112)$ GB show a least-density volume at the GB which is observable as an atomic-scale hole [see Fig. 8(d)]. With an increase in the tensile strain, this hole quickly enlarges at atomic dimensions, and the remaining Fe-Fe bonds at the GB are elastically elongated. One striking observation is that the Fe-Fe bonds around the two- $\text{V}^{\text{Fe}}\text{H}_2$ s are already relaxed even before the fracture, and the elastic elongations of bonds are concentrated spatially on just some limited number of atoms at the GB. Thus a macroscopic concept of stress/strain concentration at a crack or hole is valid even for V^{Fe} -related defects, which have small holes, with sizes less than a nanometer. This behavior is seen also for the single- $\text{V}^{\text{Fe}}\text{H}_2$ defect at the GB [see Fig. 8(c)], and

its effect is smaller than that of the two- $\text{V}^{\text{Fe}}\text{H}_2$, indicating that accumulated clusters of V^{Fe} -related defects at GBs make the strength significantly worse.

IV. RESULTS OF $\Sigma 3(111)$ GRAIN BOUNDARY

A. Interstitial hydrogen

We performed similar studies for the $\Sigma 3(111)$ GB models. Figure 9 shows calculated formation energies E^f of a single H^{int} as a function of distance from GB. The result shows that E^f becomes lower as H^{int} approaches to GB. The O site at GB is the most stable for H^{int} , where E^f is about $0.4 \text{ eV}/\text{H}^{\text{int}}$ lower than the bulk T site, consistent with the previous report by Yamaguchi *et al.*¹⁶

Figure 10 shows calculated formation energies of H^{int} as a function of number of trapped- H^{int} at $\Sigma 3(111)$ GB. The E^f values up to eight H^{int} atoms/cell are lower than that of H_2 molecule, and the E^f values up to twelve H^{int} atoms/cell are lower than that of the bulk T site. Thus even if we set a strict condition, we can estimate that eight H^{int} /cell (area density $14.4 \text{ atom}/\text{nm}^2$) can be readily trapped at the GB O -sites.

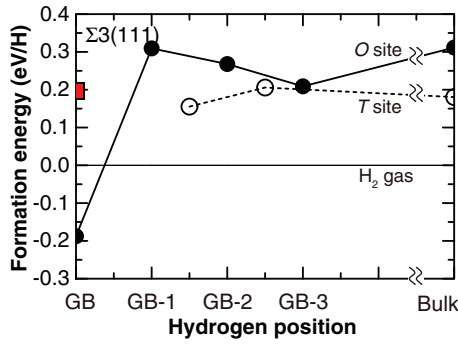


FIG. 9. (Color online) Formation energies of a single interstitial hydrogen (H^{int}) at $\Sigma 3(111)$ grain boundary. Closed and open circles are for H^{int} in octahedral (O) and tetrahedral (T) positions, respectively, and the square at the GB layer is for H^{int} at the center of the inherent open space.

Figure 11 shows effects of single, four, and eight H^{int} atoms/cell on the energy-strain and stress-strain curves at $\Sigma 3(111)$ GB calculated by the tensile tests. The effect of the single H^{int} on σ_{max} is very small, and σ_{max} values are lowered by 1% and 8% by $4H^{int}$ and $8H^{int}$, respectively, relative to the pristine $\Sigma 3(111)$ GB ($\sigma_{max} = 22.3$ GPa). The work of fracture clearly decrease with increasing number of H^{int} at GB, and elastic modulus before the fracture slightly increase but look as nearly unchanged. These results show that influences of H^{int} on the $\Sigma 3(111)$ GB has a similar character to that on the $\Sigma 3(112)$ GB case.

Figures 12(a) and 12(b) show calculated charge densities of the pristine and $8H^{int}$ -trapped $\Sigma 3(111)$ GB models under strains, respectively. In the pristine GB, the charge densities show that the intrinsic voids at the GB become wider with increasing the tensile strain. Similar to the pristine case, the intrinsic-void regions at the H^{int} -trapped GB become wider as strain increases as seen in Fig. 12(b). H atoms occupy the GB O -sites, and there are additional Fe- H^{int} -Fe bonds connecting the GB. As a result, the strength change induced by H^{int} is similar in nature to the $\Sigma 3(112)$ GB case.

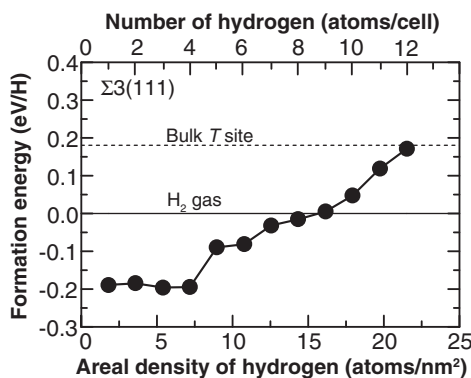


FIG. 10. Lowest formation energies of an interstitial hydrogen (H^{int}) vs number of trapped H^{int} at the $\Sigma 3(111)$ grain boundary. Upper and lower scales show the number of H^{int} per unit cell (H atoms/cell) and the areal number density of H^{int} (H atoms/nm²), respectively.

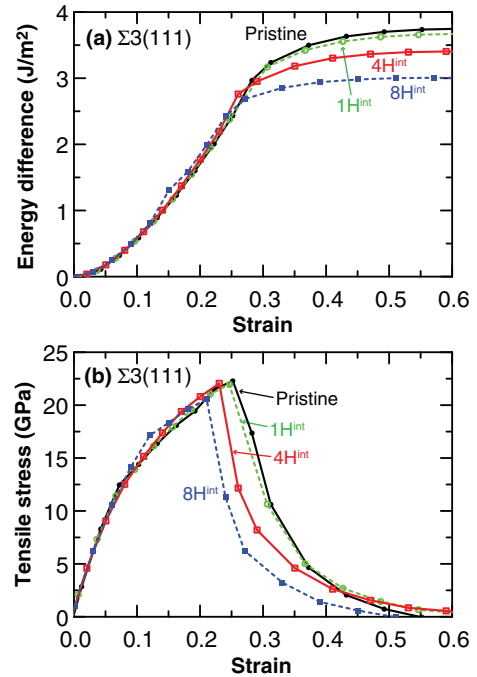


FIG. 11. (Color online) Results of tensile-test calculations for the pristine (solid line with solid circles, black), $1H^{int}$ - (broken line with open circles, green), $4H^{int}$ - (solid line with open squares, red) and $8H^{int}$ -trapped (broken line with solid squares, red) $\Sigma 3(111)$ grain boundaries: (a) energy difference relative to the equilibrium and (b) tensile stress vs uniaxial tensile strain.

B. Vacancy-hydrogen defect complexes

Figure 13 shows calculated E^f values of $V^{Fe}H_n$ ($n = 0-2$) defects at $\Sigma 3(111)$ GB. E^f near GB are much lower than the bulk values, and the lowest E^f s of all the $V^{Fe}H_n$ defects have negative values. The primary reason for the low E^f is that the GB-1 Fe-atoms across GB are very close to the Fe-Fe distance of 2.14 Å in the pristine $\Sigma 3(111)$ GB, that is shorter than that of the bulk 2.46 Å. Thus the removal of a GB-1 Fe atom is easier than the bulk and $\Sigma 3(112)$ case, and structure relaxations around V^{Fe} after the removal of Fe further reduce the E^f values. Therefore all the V^{Fe} -related defects are powerfully attracted to the $\Sigma 3(111)$ GB.

In case of the $\Sigma 3(111)$, we found significant atomic-structure relaxations induced by V^{Fe} as shown in Fig. 14. The V^{Fe} without H causes a barrier-free structure reconstruction of the GB, indicating a vacancy absorber behavior. By absorbing the V^{Fe} , the GB plane is shifted and the Fe atoms neighboring to V^{Fe} shrink with a bond rearrangement that makes the triangular structural unit shown on the right side of Fig. 14(a). Consequently, the V^{Fe} does not result in much change in the stress-strain character relative to the pristine GB, as shown in Fig. 15. Because the number of Fe atoms is reduced at the reconstructed GB, there is a lower charge-density space near GB [see Fig. 12(c)]. The low-density space becomes open with increasing strain, that is similar to a behavior of the intrinsic space in the pristine $\Sigma 3(111)$ GB. As a result, the grain boundary strength is not enhanced relative to the original $\Sigma 3(111)$.

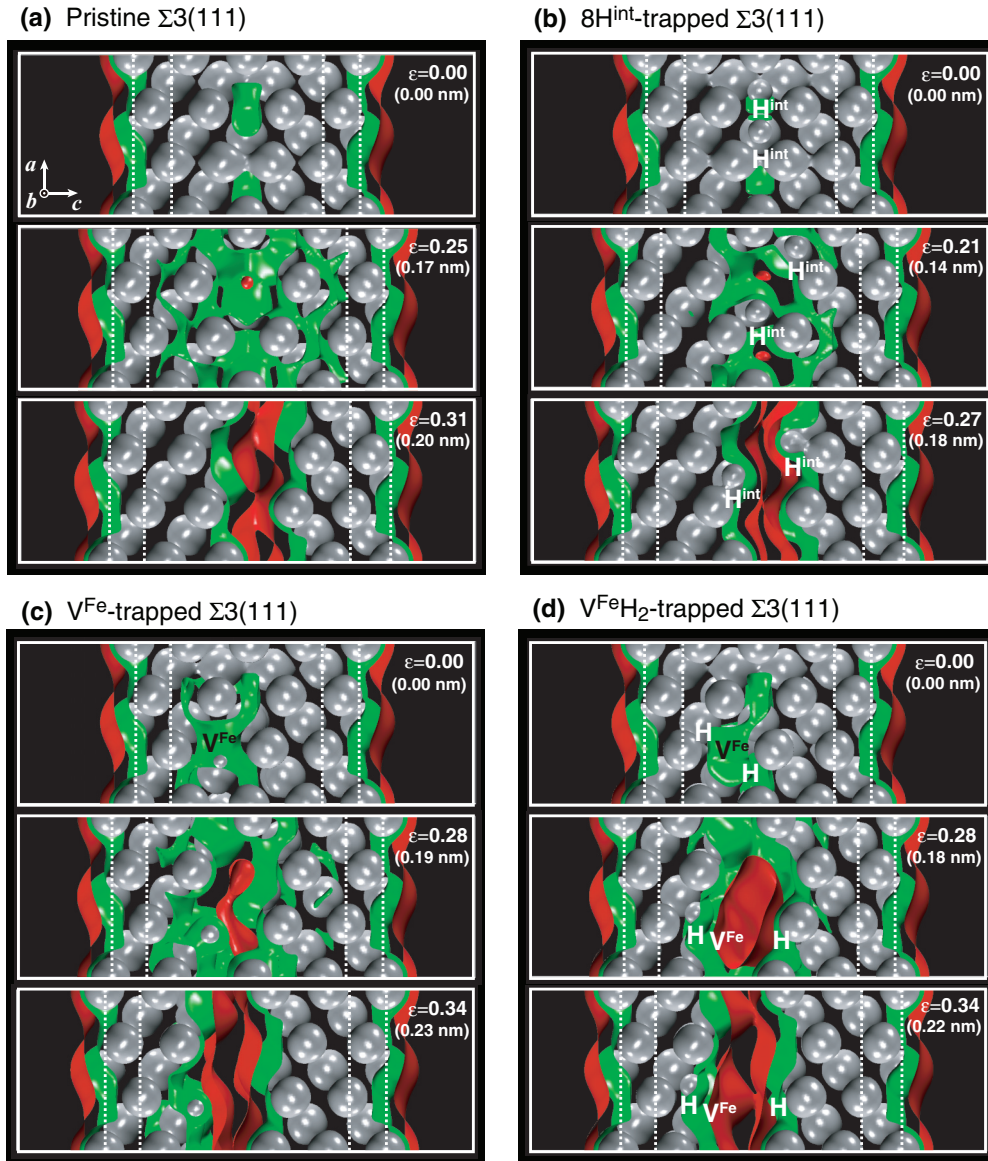


FIG. 12. (Color online) Charge densities under static uniaxial tensile strains of (a) the pristine, (b) eight H^{int} , (c) a single V^{Fe} , and (d) a single $V^{Fe}H_2$ trapped $\Sigma 3(111)$ grain boundaries. Three isosurfaces of 0.05 (red), 0.2 (green), and $0.5 e/\text{\AA}^3$ (gray) are plotted. Tensile strain (ϵ) is indicated on each panel with the displaced distance (d) of the grips (dotted lines) measured from the equilibrium position.

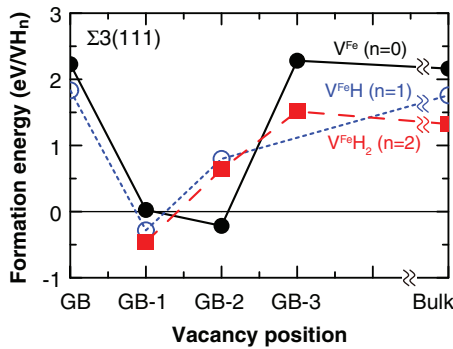


FIG. 13. (Color online) Formation energies of vacancy-hydrogen point-defect complexes $V^{Fe}H_n$ ($n = 0-2$) at the $\Sigma 3(111)$ grain boundary. Closed circles (black), open circles (blue), and squares (red) are for $n = 0, 1,$ and $2,$ respectively.

In the presence of H, however, the $V^{Fe}H_2$ and the $V^{Fe}H$ complexes are structurally quenched, becoming rigid and stable, and all the Fe atoms at the GB do not move much from their original positions in the pristine GB [see Fig. 14(b)], indicating that H is a potential obstacle to the annihilation of V^{Fe} at GBs. As a result, the $V^{Fe}H_2$ significantly reduces the σ_{max} by 23% (see Fig. 15), with similar mechanism to the $\Sigma 3(112)$ GB case as also seen in charge densities under strains [see Fig. 12(d)]. The result for the $\Sigma 3(111)$ GB shows that the joint effect of H and V^{Fe} is more pronounced on the GB weakening than on the individual respective point defects.

As shown in Fig. 6(a), we find that V^{Fe} at the $\Sigma 3(111)$ is also stabilized by trapping H^{int} s that come from bulk. However, Fig. 6(b) shows a special behavior of the V^{Fe} -related defects at the $\Sigma 3(111)$, indicating that separated V^{Fe} and $2H^{int}$ are slightly more stable than $V^{Fe}H_2$. Thus $V^{Fe}H_2$ at $\Sigma 3(111)$

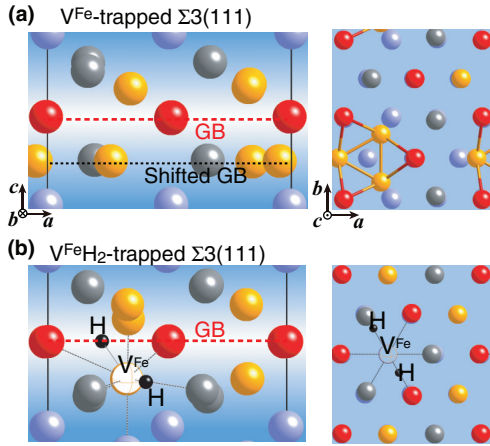


FIG. 14. (Color online) Atomic structures at (a) V^{Fe} - and (b) $V^{\text{Fe}}\text{H}_2$ -trapped $\Sigma 3(111)$ grain boundaries. V^{Fe} induces the GB structure reconstruction mainly due to large atomic relaxations of GB-1 and GB-2 atoms (yellow and gray spheres) as seen in (a), but atomic structure relaxations near the $V^{\text{Fe}}\text{H}_2$ are relatively small as shown in (b).

will release H atoms to the GB O sites to decrease the grain-boundary energy gained by the structure reconstruction induced by V^{Fe} . If a vacancy concentration is high enough near GBs, the local structure-reconstruction at GB induced by vacancies will be further promoted until a grain-boundary energy reaches an energy minimum.

Table IV lists the cell-size dependence on E^f of a single V^{Fe} for $\Sigma 3(112)$ and $\Sigma 3(111)$ GB supercell models composed

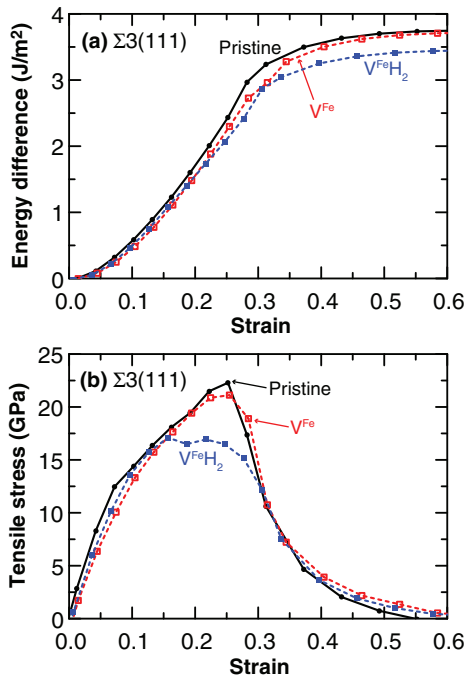


FIG. 15. (Color online) Results of tensile-test calculations for the pristine (solid line with circles, black), V^{Fe} - (broken line with open squares, red) and $V^{\text{Fe}}\text{H}_2$ -trapped (broken line with solid squares, blue) $\Sigma 3(111)$ grain boundaries: (a) energy difference relative to the equilibrium and (b) tensile stress vs uniaxial tensile strain.

TABLE IV. Calculated formation energies of a single vacancy $E^f(V^{\text{Fe}})$ (eV/ V^{Fe}) in $\Sigma 3(112)$ and $\Sigma 3(111)$ grain-boundary supercell models composed of a number of atoms (N) of 48, 96, and 192 atoms/cell. The 48- and 192-atom supercells have half and twice of the grain-boundary area per cell (S_{GB}) of the 96-atom supercell described in Sec. II A, respectively.

N (atom/cell)	S_{GB} ($\text{\AA}^2/\text{cell}$)	$E^f(V^{\text{Fe}})$ at GB-1	$E^f(V^{\text{Fe}})$ at GB-2
$\Sigma 3(112)$			
48	19.72	1.72	
96	39.43	1.73	1.80
192	78.86	1.79	
$\Sigma 3(111)$			
48	27.88	0.07	0.03
96	55.76	0.03	-0.22
192	111.52	0.05	-0.31

of 48, 96, and 192 atoms/cell. The supercell models of 48 and 192 atom/cell have half and twice GB area of the 96-atom model described in Sec. II A. The cell-size dependence on E^f values is rather small for $\Sigma 3(112)$ within 0.07 eV/ V^{Fe} , and V^{Fe} at GB-1 for $\Sigma 3(111)$ show positive values within the 0.04 eV/ V^{Fe} difference depending on the supercells.

V^{Fe} at GB-2 in the 192- and 96-atom $\Sigma 3(111)$ models, corresponding to the areal V^{Fe} -density of 0.9 and 1.8 $V^{\text{Fe}}/\text{nm}^2$, show negative E^f . The negative E^f contribute to reduce the grain boundary energy γ_{GB} of $\Sigma 3(111)$. The calculated γ_{GB} of the 192- and 96-atom cell with V^{Fe} are 1.62 and 1.60 J/ m^2 , respectively, which is lower than γ_{GB} of the pristine $\Sigma 3(111)$ of 1.66 J/ m^2 . We also found in the 192-atom cell, the triangular structural unit is made at the V^{Fe} position, but the formations of triangular structural unit are not possible in the 48-atom cell because atomic relaxations of Fe atoms neighboring to V^{Fe} are restricted due to its high V^{Fe} -density within the orthorhombic cell shape. Thus γ_{GB} of $\Sigma 3(111)$ may further decrease by maximizing the density of the triangular structural units.

We further studied the defect stabilities by modeling a fully reconstructed $\Sigma 3(111)$ GB with a hexagonal supercell (see Fig. 16), which is generated in a way to be a higher density of the triangular local-structural unit in the GB plane. The atomic structures of the model are fully relaxed by

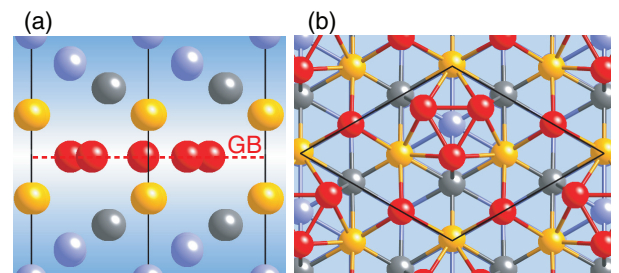


FIG. 16. (Color online) Local atomic structure of the fully reconstructed $\Sigma 3(111)$ grain boundary (GB) model, which is generated in a way to be a higher density of the triangular structural unit in the GB plane using the hexagonal 70-atom unit cell. Atomic structures are optimized from first principles. The calculated GB energy of this model is 1.52 J/ m^2 , which is lower than the original $\Sigma 3(111)$ GB (1.66 J/ m^2).

first-principles calculations until the forces acting on atoms become negligible. The model is a hexagonal cell and has 70 Fe atoms per unit cell, which has the GB area of 41.82 \AA^2 . The calculated GB energy of the fully reconstructed model is 1.52 J/m^2 , which is lower than the original $\Sigma 3(111)$ GB (1.66 J/m^2). The calculated lowest E^f of H^{int} and $\text{V}^{\text{Fe}}\text{H}_n$ ($n = 0-2$) defects at the fully reconstructed $\Sigma 3(111)$ model are listed in Table III. The E^f values of all the defects in the fully reconstructed model are higher than that of the original $\Sigma 3(111)$, but lower than those at the $\Sigma 3(112)$. Figure 6 shows what interactions act between 1V^{Fe} and 2H , and the fully reconstructed model shows that V^{Fe} is stabilized by trapping H atoms, similar to the $\Sigma 3(112)$ case, supporting the idea that H stabilizes V^{Fe} at the GB.

V. DISCUSSION

Based on the results, the vacancy mechanisms could help to explain a long time delay in the development of a brittle fracture in steel. Because H is basically diffusive in Fe,³ time delays in developing damage from embrittlement might be expected to be short.¹⁴ On the other hand, the mobility of vacancies is generally much slower. Thus the V^{Fe} -related defects, which are created inside materials in association with strains and plastic deformations,^{5,22,24} will slowly and steadily accumulate at GBs, thereby producing damage that will eventually cause a brittle fracture at the GBs. A previous first-principles study has shown a V^{Fe} migration energy of 0.65 eV in bulk α -Fe, which is close to an experimental value 0.55 eV .⁴⁵ Interestingly, recent computational study shows that the V^{Fe} migration energies along GBs become smaller than that in the bulk.³³

In addition, our results show that the formation-energy differences between the two GBs are about 1.5 eV and about 0.1 eV for the $\text{V}^{\text{Fe}}\text{H}_2$ and the H^{int} , indicating that they are respectively sensitive, and insensitive, to the type of

GB. Although direct comparisons are difficult, intergranular cracks are experimentally known to be sensitive to GBs in Fe.^{2,11,12} A certain amount of H^{int} can be trapped at most GBs, and H^{int} should have an influence on the overall material if H^{int} is insensitive to the type of GB. On the other hand, the V^{Fe} -related defects would selectively attack susceptible GBs inside a material, and the GBs would lead to a brittle failure.

VI. CONCLUSION

We have investigated atomistic mechanisms of hydrogen embrittlement with vacancies at grain boundaries in α -Fe from first-principles calculations. We evaluate the influence of defects in α -iron on mechanical strength under static tensile loadings, and find that hydrogen and vacancies accumulate as defect complexes at grain boundaries, thereby decreasing tensile strength. This effect of defect complexes is found to be much worse for the grain boundary strength than the effect of each factor, and hydrogen promotes the activities of vacancies at grain boundaries. Because of the low mobility of vacancies, this mechanism can account for the delayed brittle fractures induced by hydrogen in steel.

ACKNOWLEDGMENTS

This study was partly supported by the RISS project of MEXT and the MEXT Program for Development of Environment Technology using Nanotechnology of the Japanese Government. The computation in this work has been done using the Numerical Materials Simulator, National Institute for Materials Science, Japan, the Supercomputing Division, Information Technology Center, University of Tokyo, Japan, and the facilities of the Supercomputer Center, Institute for Solid State Physics, University of Tokyo, Japan.

*momida@sanken.osaka-u.ac.jp

[†]Present address: Central Research Laboratory, Hitachi, Ltd., 2520 Akanuma, Hatoyama, Saitama 350-0395, Japan.

[‡]Present address: Department of General Science, Hachinohe National College of Technology, 16-1 Uwanotai, Tamonoki, Hachinohe, Aomori 039-1192, Japan.

§ohno.takahisa@nims.go.jp

¹H. C. Rogers, *Science* **159**, 1057 (1968).

²R. A. Oriani, *Ann. Rev. Mater. Sci.* **8**, 327 (1978).

³J. P. Hirth, *Metall. Trans. A* **11**, 861 (1980).

⁴S. M. Myers, M. I. Baskes, H. K. Birnbaum, J. W. Corbett, G. G. DeLeo, S. K. Estreicher, E. E. Haller, P. Jena, N. M. Johnson, R. Kirchheim, S. J. Pearton, and M. J. Stavola, *Rev. Mod. Phys.* **64**, 559 (1992).

⁵M. Nagumo, *Mater. Sci. Technol.* **20**, 940 (2004).

⁶K. H. Lo, C. H. Shek, and J. K. L. Lai, *Mater. Sci. Eng. R* **65**, 39 (2009).

⁷H. K. Birnbaum and P. Sofronis, *Mater. Sci. Eng. A* **176**, 191 (1994).

⁸R. A. Oriani and P. H. Josephic, *Acta Metall.* **22**, 1065 (1974).

⁹S. Serebrinsky, E. A. Carter, and M. Ortiz, *J. Mech. Phys. Solids* **52**, 2403 (2004).

¹⁰For example, M. Wang, E. Akiyama, and K. Tsuzaki, *Scr. Mater.* **52**, 403 (2005).

¹¹I. M. Bernstein, *Metall. Trans.* **1**, 3143 (1970).

¹²B. B. Rath and I. M. Bernstein, *Metall. Trans.* **2**, 2979 (1971).

¹³J. R. Rice and J.-S. Wang, *Mater. Sci. Eng. A* **107**, 23 (1989).

¹⁴N. J. Petch and P. Stables, *Nature (London)* **169**, 842 (1952).

¹⁵L. Zhong, R. Wu, A. J. Freeman, and G. B. Olson, *Phys. Rev. B* **62**, 13938 (2000).

¹⁶M. Yamaguchi, K. Ebihara, M. Itakura, T. Kadoyoshi, T. Suzudo, and H. Kaburaki, *Metall. Mater. Trans. A* **42**, 330 (2011).

¹⁷M. Yamaguchi, J. Kameda, K. Ebihara, M. Itakura, and H. Kaburaki, *Philos. Mag.* **92**, 1349 (2012).

¹⁸Y. A. Du, L. Ismer, J. Rogal, T. Hickel, J. Neugebauer, and R. Drautz, *Phys. Rev. B* **84**, 144121 (2011).

¹⁹M. Nagumo, M. Nakamura, and K. Takai, *Metall. Mater. Trans. A* **32**, 339 (2001).

- ²⁰M. Iwamoto and Y. Fukai, *Mater. Trans. JIM* **40**, 606 (1999).
- ²¹Y. Fukai, *Phys. Scr. T* **103**, 11 (2003).
- ²²K. Sakaki, T. Kawase, M. Hirato, M. Mizuno, H. Araki, Y. Shirai, and M. Nagumo, *Scr. Mater.* **55**, 1031 (2006).
- ²³H. Fuchigami, H. Minami, and M. Nagumo, *Philos. Mag. Lett.* **86**, 21 (2006).
- ²⁴K. Takai, H. Shoda, H. Suzuki, and M. Nagumo, *Acta Mater.* **56**, 5158 (2008).
- ²⁵Y. Tateyama and T. Ohno, *Phys. Rev. B* **67**, 174105 (2003).
- ²⁶Y. Tateyama and T. Ohno, *ISIJ Int.* **43**, 573 (2003).
- ²⁷W.-T. Geng, A. J. Freeman, G. B. Olson, Y. Tateyama, and T. Ohno, *Mater. Trans.* **46**, 756 (2005).
- ²⁸G. Lu and E. Kaxiras, *Phys. Rev. Lett.* **94**, 155501 (2005).
- ²⁹P. R. Monasterio, T. T. Lau, S. Yip, and K. J. Van Vliet, *Phys. Rev. Lett.* **103**, 085501 (2009).
- ³⁰R. Nazarov, T. Hickel, and J. Neugebauer, *Phys. Rev. B* **82**, 224104 (2010).
- ³¹M. A. Tschopp, K. N. Solanki, F. Gao, X. Sun, M. A. Khaleel, and M. F. Horstemeyer, *Phys. Rev. B* **85**, 064108 (2012).
- ³²H.-B. Zhou, Y.-L. Liu, C. Duan, S. Jin, Y. Zhang, F. Gao, X. Shu, and G.-H. Lu, *J. Appl. Phys.* **109**, 113512 (2011).
- ³³F. Gao, H. L. Heinisch, and R. J. Kurtz, *J. Nucl. Mater.* **386–388**, 390 (2009).
- ³⁴H. Nakashima and M. Takeuchi, *Tetsu to Hagane* **86**, 357 (2000).
- ³⁵P. Hohenberg and W. Kohn, *Phys. Rev.* **136**, B864 (1964).
- ³⁶W. Kohn and L. J. Sham, *Phys. Rev.* **140**, A1133 (1965).
- ³⁷J. P. Perdew, K. Burke, and M. Ernzerhof, *Phys. Rev. Lett.* **77**, 3865 (1996); **78**, 1396(E) (1997).
- ³⁸P. E. Blöchl, *Phys. Rev. B* **50**, 17953 (1994).
- ³⁹G. Kresse and D. Joubert, *Phys. Rev. B* **59**, 1758 (1999).
- ⁴⁰J. Hafner, *J. Comput. Chem.* **29**, 2044 (2008).
- ⁴¹G. Kresse and J. Furthmüller, *Phys. Rev. B* **54**, 11169 (1996).
- ⁴²M. Methfessel and A. T. Paxton, *Phys. Rev. B* **40**, 3616 (1989).
- ⁴³W. Humphrey, A. Dalke, and K. Schulten, *J. Molec. Graphics* **14**, 33 (1996).
- ⁴⁴S. K. Bhattacharya, S. Tanaka, Y. Shiihara, and M. Kohyama, *J. Phys.: Condens. Matter* **25**, 135004 (2013).
- ⁴⁵C. Domain and C. S. Becquart, *Phys. Rev. B* **65**, 024103 (2001).
- ⁴⁶D. E. Jiang and E. A. Carter, *Phys. Rev. B* **70**, 064102 (2004).
- ⁴⁷C. Kittel, *Introduction to Solid State Physics*, 6th ed. (Wiley, New York, 1987).
- ⁴⁸H. Danan, A. Herr, and A. J. P. Meyer, *J. Appl. Phys.* **39**, 669 (1968).
- ⁴⁹L. De Schepper, D. Segers, L. Dorikens-Vanpraet, M. Dorikens, G. Knuyt, L. M. Stals, and P. Moser, *Phys. Rev. B* **27**, 5257 (1983).
- ⁵⁰H. Schultz, *Mater. Sci. Eng. A* **141**, 149 (1991).
- ⁵¹J. Wolff, M. Franz, and T. Hehenkamp, *Mikrochim. Acta* **125**, 263 (1997).
- ⁵²S. Ogata, J. Li, and S. Yip, *Science* **298**, 807 (2002).
- ⁵³R. Schweinfest, A. T. Paxton, and M. W. Finnis, *Nature (London)* **432**, 1008 (2004).
- ⁵⁴M. Yamaguchi, M. Shiga, and H. Kaburaki, *Science* **307**, 393 (2005).
- ⁵⁵S. Zhang, O. Y. Kontsevoi, A. J. Freeman, and G. B. Olson, *Phys. Rev. B* **82**, 224107 (2010).
- ⁵⁶M. Friák, M. Šob, and V. Vitek, *Philos. Mag.* **83**, 3529 (2003).
- ⁵⁷M. Černý and J. Pokluda, *Phys. Rev. B* **82**, 174106 (2010).
- ⁵⁸R. Wu, A. J. Freeman, and G. B. Olson, *Science* **265**, 376 (1994).
- ⁵⁹A. Y. Lozovoi, A. T. Paxton, and M. W. Finnis, *Phys. Rev. B* **74**, 155416 (2006).